Spectral-Domain Optical Coherence Tomography Enhanced Depth Imaging of the Normal and Glaucomatous Nonhuman Primate Optic Nerve Head

Hongli Yang,[1,2] *Jingjing Qi,*[2,3] *Christy Hardin,*[1] *Stuart K. Gardiner,*[1] *Nicholas G. Strouthidis,*[4] *Brad Fortune,*[1] *and Claude F. Burgoyne*[1]

Purpose. To test whether the enhanced depth imaging (EDI) modality improves anterior and posterior lamina cribrosa surface (ALCS and PLCS) visibility compared with conventional spectral-domain optical coherence tomography (SD-OCT).

Methods. Conventional and EDI SD-OCT scans were obtained 30 minutes after IOP was manometrically lowered to 10 mm Hg in both eyes of 14 nonhuman primates (NHPs) with unilateral experimental glaucoma (EG). Thirteen horizontal and seven vertical radial B-scans of each SD-OCT data set were delineated by one operator masked to image type. Delineated ALCS and PLCS points were projected to 1 of 100 equal-sized subregions of the neural canal opening (NCO) reference plane, and the number of delineated subregions (≥2 points) was counted. Poisson regression was used to analyze the effects of image type, treatment, and quadrant. Two additional delineations were performed for three NHPs to compare reproducibility.

Results. EDI increased the number of subregions delineated for both the ALCS (by 28%; $P < 0.0001$) and PLCS (by 225%; $P < 0.0001$). EDI improvement in ALCS visibility was significant in the superior quadrant only and was not different in EG versus control eyes, whereas EDI improvement in PLCS visibility was significant in all four quadrants ($P < 0.005$) and greater in EG eyes ($P < 0.001$), nasally and temporally. Intradelineator reproducibility was not different between image types. EDI and standard ONH parameter values were similar except for PLCS depth which was deeper in the EDI data sets ($P = 0.0002$).

Conclusions. ALCS and PLCS visibility within control and EG NHP ONHs increased in EDI compared to conventional SD-OCT data sets. Further study of EDI effects on PLCS parameterization is required. (*Invest Ophthalmol Vis Sci.* 2012;53:394–405) DOI:10.1167/iovs.11-8244

From the [1]Devers Eye Institute, Portland, Oregon; [3]NYU Polytechnic Institute, Brooklyn, New York; and the [4]Moorfields Eye Hospital, London, United Kingdom.

[2]These authors contributed equally to the work presented here and should therefore be regarded as equivalent first authors.

Supported by National Institutes of Health Grant R01-EY11610, the Legacy Good Samaritan Foundation, Heidelberg Engineering, and Sears Medical Trust.

Submitted for publication July 19, 2011; revised October 20, 2011; accepted November 30, 2011.

Disclosure: **H. Yang**, None; **J. Qi**, None; **C. Hardin**, None; **S.K. Gardiner**, None; **N.G. Strouthidis**, None; **B. Fortune**, Heidelberg Engineering (F); **C.F. Burgoyne**, Heidelberg Engineering (F, R)

Corresponding author: Claude F. Burgoyne, Optic Nerve Head Research Laboratory, Devers Eye Institute, Legacy Health System, 1225 NE Second Avenue, PO Box 3950, Portland, OR 97208-3950; cfburgoyne@deverseye.org.

Previous studies of human and experimental glaucoma (EG) suggest that optic nerve head (ONH) structural change within the peripapillary sclera, lamina cribrosa, and prelaminar neural tissues is associated with early axonal injury.[1–7] Lamina cribrosa alterations in human glaucomatous eyes have been reported to include posterior deformation,[2,8] compression and thinning,[4,8,9] and molecular changes in astrocytes and other glial cells.[10,11] Our studies in early NHP EG, in which we used histomorphometric methods, demonstrate posterior deformation and thickening of the lamina cribrosa and prelaminar neural tissues,[12–14] laminar beam and pore size alterations (Grimm J, et al. *IOVS* 2007;48:ARVO E-Abstract 3295) and posterior migration of both the anterior and posterior laminar insertions from the sclera toward and sometimes into the pial sheath.[15] Taken together, these studies emphasize the importance of clinical visualization of the deep optic nerve head neural and connective tissues, particularly if that visualization can be achieved without diminishing the quality of prelaminar and peripapillary retinal nerve fiber layer (RNFL) quantification.

Spectral-domain optical coherence tomography (SD-OCT) has been shown to enable reproducible quantification of the macular ganglion cell complex,[16,17] the peripapillary RNFL and retina.[18] It is increasingly being applied to ONH imaging.[19–24] Several reports have also demonstrated the ability of SD-OCT to visualize the human lamina cribrosa.[25,26] Inoue et al.[26] used SD-OCT imaging system to demonstrate lamina cribrosa thickness reduction in ocular hypertensive and glaucoma patients in a cross-sectional study. Agoumi et al.[27] used a clinical SD-OCT imaging device to study the effect of acute IOP changes in 36 human subjects.

We have previously demonstrated SD-OCT visualization and quantification of the ONH tissues and peripapillary RNFL in rhesus NHPs. These studies have included a description of the important components of SD-OCT-detected optic disc margin anatomy[28]; confirmation of SD-OCT ONH anatomy in serial B-scans co-localized to serial histologic sections[29]; demonstration of detectable but clinically insignificant thinning of the peripapillary RNFL thickness (RNFLT) after acute IOP elevation[30]; detection of prelaminar neural tissue and Bruch's membrane deformation with only infrequent lamina cribrosa deformation after acute IOP elevation[31]; and a description of a novel set of ONH and peripapillary RNFL parameters and their use in longitudinal ONH change detection using SD-OCT in NHP experimental glaucoma.[20] However, all of our studies to date have used an SD-OCT device with a conventional 870-nm center wavelength source without enhanced depth imaging (EDI), and only the anterior lamina cribrosa surface (ALCS) could be reliably visualized in most normal and EG NHP eyes.

In conventional SD-OCT imaging, the solution to the Fourier transform of the detected spectrum for each A-scan is symmetric about the point of 0 delay (relative to the flight time of the reference beam) because positive and negative delays are typ-

ically not disambiguated. In clinical devices, the resultant B-scan is typically trimmed so that only the upright half of each B-scan is portrayed (corresponding to positive delays). There is a well-known roll-off of sensitivity with increasing frequency corresponding to increasing delays or depth of reflections within the sample. Known as depth degeneracy, this phenomenon limits detection of structural detail at increasing depths within the sample tissue. By intentionally manipulating the depth of the sample relative to the reference arm—that is, by pushing the sample closer to the 0 delay point and beyond—it is possible to take advantage of the above-mentioned ambiguity. The B-scan images appear to invert (flip around the 0 delay line), such that the deeper portions of the sample lie closer to the 0 delay line and depth degeneracy causes loss of sensitivity for the more anterior portions of the sample. Importantly, the increased sensitivity at the lower frequencies now corresponds to the deeper portions of the sample, which may allow greater detail to be detected for deeper tissue structures.

Spaide et al.[32] were the first to publish these observations in the context of imaging structures deeper than the retina, such as the choroid and sclera. Additional reports have described enhanced visualization of these structures within the macular region.[32–35] More recently, it has been used to enhance visualization of the lamina cribrosa within the ONH.[36] (Qi J, et al. *IOVS* 2011;52:ARVO E-Abstract 166). The Spectralis SD-OCT (Heidelberg Engineering GmbH, Heidelberg, Germany) now includes as part of its software suite the Enhanced Depth Imaging (EDI) mode, which, once engaged, changes the position of the reference arm so that the enhanced depth image is acquired at the same position as the conventional image and no longer appears inverted during acquisition.

The purpose of the present study was to quantitatively test the hypothesis that anterior (ALCS) and posterior lamina cribrosa surface (PLCS) visualization is enhanced by EDI compared with conventional SD-OCT data sets. Our secondary purpose was to determine whether the sensitivity roll-off (depth-degeneracy), operating in the inverse direction in the EDI mode, would be detrimental to quantifying the more anterior structures.

Methods

Animals

The Legacy Health Institutional Animal Care and Use Committee approved all aspects of this study. All animals were treated in accordance with the ARVO Statement for the Use of Animals in Ophthalmic and Vision Research. As part of other ongoing longitudinal studies, both eyes of 14 rhesus macaque nonhuman primate (NHPs) (*Macaca mulatta*) with chronic, unilateral EG[14] were imaged on a single occasion, which occurred at various intervals after commencement of trabecular meshwork laser treatments[37] in the EG eyes. The 14 EG eyes were therefore imaged at various stages of EG damage (Table 1, rightmost column).

Imaging Protocol

All ophthalmic imaging sessions began with induction of general anesthesia with ketamine (15 mg/kg, by intramuscular injection) and midazolam (0.2 mg/kg, by intramuscular injection) accompanied by a single subcutaneous injection of atropine sulfate (0.05 mg/kg). Animals were then intubated and maintained on 100% oxygen and isoflurane gas (1%–2%), typically 1.25%, and intravenous fluids (lactated Ringer's solution, 10 mL/kg/h and/or 6% hetastarch) were then administered via the saphenous vein. One drop of topical corneal anesthetic was placed in each eye (0.5% proparacaine), a lid speculum was inserted, and intraocular pressure (IOP) was measured by applanation tonometry (Tonopen XL; Reichert, Depew, NY) and reported as the average of three or more measurements. Pupillary dilation was induced with one

Table 1. Demographics, IOP Characteristics and SD-OCT Circle Scan RNFLT Data for Each Study Animal

Animal	Animal ID	Sex	Age (y)	Weight (kg)	Time of Imaging Session (wk after Laser)	Cumulative IOP Difference* (mm Hg day)	Baseline Mean IOP N/EG (mm Hg)	EG Eye Peak Post-laser IOP (mm Hg)	Mean RNFLT N//EG at Baseline† (μm)	Mean RNFLT N//EG at EDI Image Session‡ (μm)
1	15527	F	22	8.4	1.9	−62*	11/11	16	98/102	99/106
2	24369	F	6	6.7	3.1	−37*	11/11	14	100/95	94/101
3	22165	F	22	6.8	12.4	55	9/9	13	92/91	94/98
4	23522	F	12	7.0	12.4	128	10/10	16	91/95	89/94
5	22100	F	23	6.3	10.1	148	9/10	19	85/86	90/88
6	22159	F	20	8.1	13.3	202	8/9	18	92/95	91/94
7	23532	F	12	5.0	8.9	402	11/12	32	86/83	86/77
8	26163	M	4	6.5	16.9	557	8/8	21	100/99	106/108
9	23506	F	13	4.5	8.0	713	12/12	49	90/90	100/85
10	25356	M	5	5.6	17.3	991	8/7	41	116/114	118.5/119
11	22906	F	14	8.0	75.9	4675	9/11	48	103/102	106/100
12	20655	F	11	6.0	120.0	7006	11/12	50	NA/NA	83/35
13	23534	F	12	4.2	113.9	10640	12/12	41	88/85	94/61
14	21808	F	10	7.2	121.0	11599	15/14	47	NA/NA	101/68

* Negative values suggest that postlaser-detected IOPs in the glaucomatous eye were not yet elevated and in fact were lower than in the normal eye, which is not uncommon in the early postlaser period.

† The average of SD-OCT conventional circle scan RNFLT in the baseline sessions before the laser treatment.

‡ The mean SD-OCT on EDI image day. SD-OCT conventional circle RNFLT on the day when both the conventional and EDI radial data sets were obtained.

drop each of tropicamide (0.5%) and phenylephrine (2.5%). A clear, plano-powered, rigid gas-permeable contact lens was placed on each eye with topical lubricant (0.5% carboxymethylcellulose sodium, Refresh; Allergan, Irvine, CA).

Intraocular pressure in both eyes was adjusted to 10 mm Hg using a manometer connected to a 27-gauge cannula, which was inserted through the temporal cornea into the anterior chamber. Imaging commenced 30 minutes after IOP stabilization at 10 mm Hg. All SD-OCT imaging was performed with a commercially available SD-OCT (Spectralis; Heidelberg Engineering, GmbH), which uses a superluminescence diode to emit a low-coherence scanning beam with a center wavelength of 870 nm. For this study, a conventional ONH 80–radial-B-scan pattern was acquired over a 30° area (768 A-scans per B-scan) followed by a conventional peripapillary RNFLT circle scan. An EDI 80–radial-scan data set was then acquired using the existing system software. All image acquisition was centered on the ONH. The device's eye tracking facility was turned on during image acquisition to enable repeated B-scan acquisition ($n = 9$) and sweep averaging in real time to reduce speckle noise. For each eye, the conventional and EDI 80 B-scan data sets were acquired relative to a single reference image ensuring that the location of each B-scan remained stable in the conventional and EDI scans.

Delineation of SD-OCT Volumes

Our technique for SD-OCT delineation of ONH has been described in detail elsewhere.[20,30] Briefly, raw SD-OCT data from each conventional

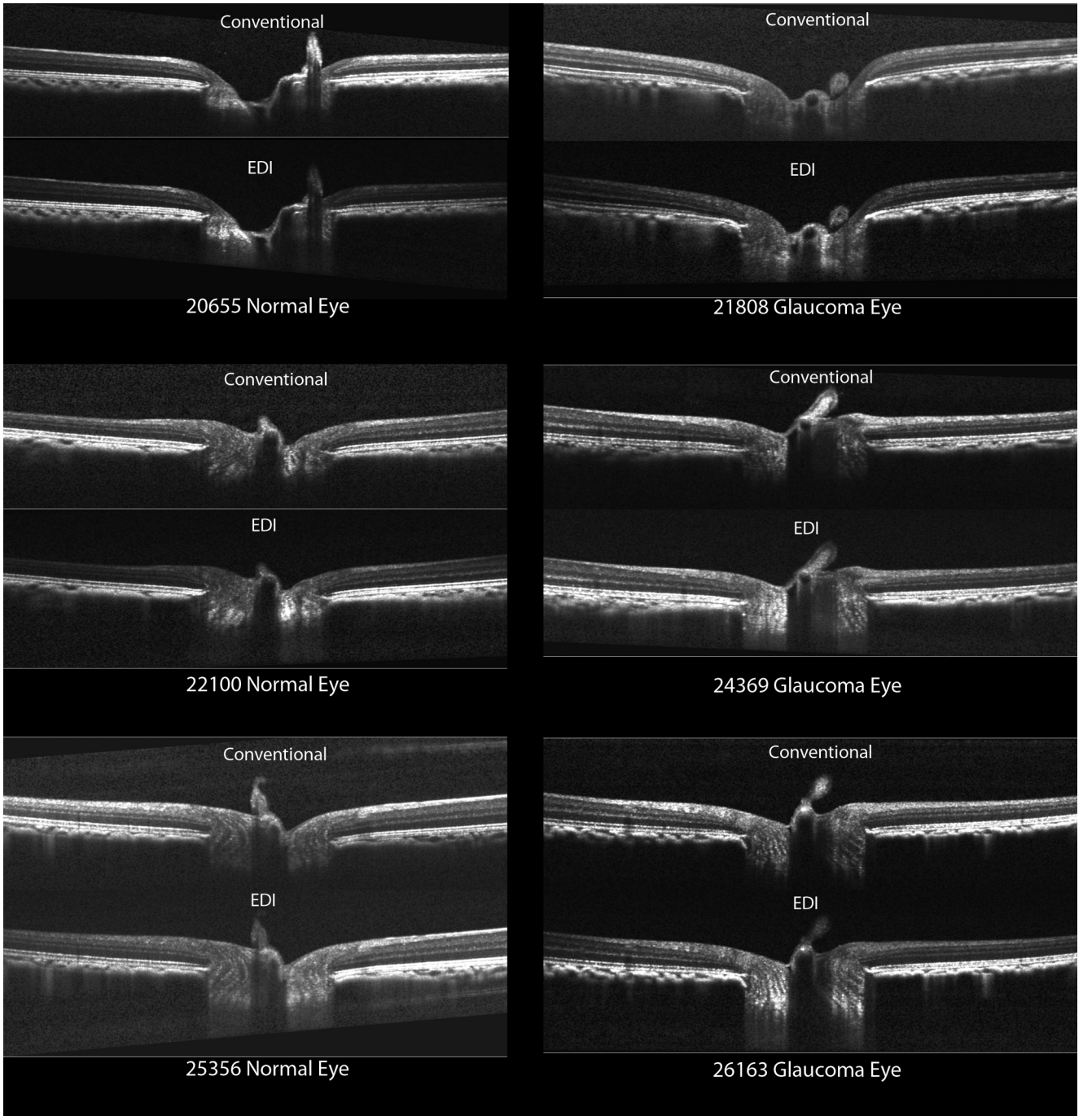

Figure 1. Conventional and EDI horizontal SD-OCT B-scans from the same location of six representative eyes.

and EDI data set (Fig. 1) were exported into our custom-built Multiview 3D visualization and delineation software (based on the Visualization Toolkit; VTK, Clifton Park, NY). ONH and peripapillary landmarks (Fig. 3) were then hand delineated in a subset of 13 horizontal and 7 vertical radial B-scans of each conventional and EDI data set (Fig. 2).

A single operator who was masked to the type of image acquisition (conventional versus EDI) and treatment status (control or EG) of the imaged ONH performed all delineations. ONH landmarks included (Fig. 3): the internal limiting membrane (ILM); posterior surface of the RNFL; posterior surface of the Bruch's membrane/retinal pigment epithelium (BM/RPE) complex; the neural canal opening (NCO), defined as the innermost end of the SD-OCT-detected BM/RPE on either side of neural canal[20]; border tissue of Elschnig (extending from the sclera to the BM/RPE complex on either side of the neural canal at the innermost termination of the choroidal signal)[20]; and the anterior scleral surface, the ALCS, and the PLCS.

Our strategy for delineating the ALCS and PLCS (Fig. 3) was based on our previous direct comparisons between SD-OCT B-scans and matched histologic sections obtained from a normal NHP eye,[29] as well as our previous publications on SD-OCT detection of longitudinal change (Yang H, et al. *IOVS* 2011;52:ARVO E-Abstract 5921).[20] Within each B-scan, we identified the ALCS as being the point where a horizontally oriented, high-intensity signal below the disc surface begins to intersect the high intensity vertical striations that we have previously identified to be the prelaminar glial columns (Fig. 3).[29] We identified the PLCS as being present where the horizontally oriented, high-density signal identified as the lamina ended. It is important to note that the signals from the ALCS and PLCS were often discontinuous in regions where there was pronounced shadowing from overlying retinal vessels. For this reason, ALCS and PLCS were delineated using discrete marks rather than using continuous Bézier curves, which is the delineation tool we use for all other surfaces.[20] The observer could employ any number of marks, at their discretion, to delineate the ALCS and/or the PLCS.

Quantification of the Extent of ALCS and PLCS Visibility in Each SD-OCT Data Set

To quantify the extent of laminar visualization in each SD-OCT data set, we projected delineated ALCS and PLCS points onto the NCO reference plane (Fig. 4). The NCO reference plane is determined by the best-fit ellipse to the 80 delineated NCO points in all 40 sections (see below).[38,39] The NCO reference plane, with the projected laminar marks was then divided into 100 equal-sized subregions, as previously described.[20] Delineated subregions (Fig. 4 shaded areas) were those that contained two or more delineated points. To assess the regional effects on laminar surface visibility, the projected NCO ellipse was divided into superior (S), inferior (I), nasal (N), and temporal (T) quadrants.

Quantification of ONH and RNFL Parameters in Each SD-OCT Data Set

To compare the value of all ONH and RNFLT parameters in the conventional and EDI data sets of each eye (Fig. 5), we rescaled all x, y dimensions in the SD-OCT output volume files (which are based on average human eye optics and dimensions) for the average NHP eye, using a scaling factor of 0.857 as described in our previous reports.[20,30] Our strategy for 3D quantification of ONH data sets is based on 40 delineated radial sections[12,38] and has been modified for SD-OCT ONH data sets, as previously described.[20,30] Because only a subset of 20 radial sections were delineated for this study, the following parameters were quantified in each of 20 delineated B-scans (Fig. 5) and their value reported as the mean ± SD: rim width, rim area, RNFLT 1200, and RNFL area.

For each data set, the NCO was delineated in the complete set of 40 radial sections (rather than the subset of 20 in which all landmarks were delineated, described above). A best-fit ellipse was determined and used as a reference plane. The following parameters were then calculated as single values for each SD-OCT data set based on the NCO best-fit ellipse: NCO ellipse area, NCO ellipse major, and NCO ellipse minor.

Finally, ALCS and PLCS depth (Fig. 5) relative to the NCO reference plane were quantified as the mean depth of the ALCS or PLCS points (relative to the NCO reference plane) for just those points that fell within delineated subregions, as outlined above.

Reproducibility

Delineations were performed two additional times (by the same delineator, 2 weeks apart) on both the conventional and EDI scans of both

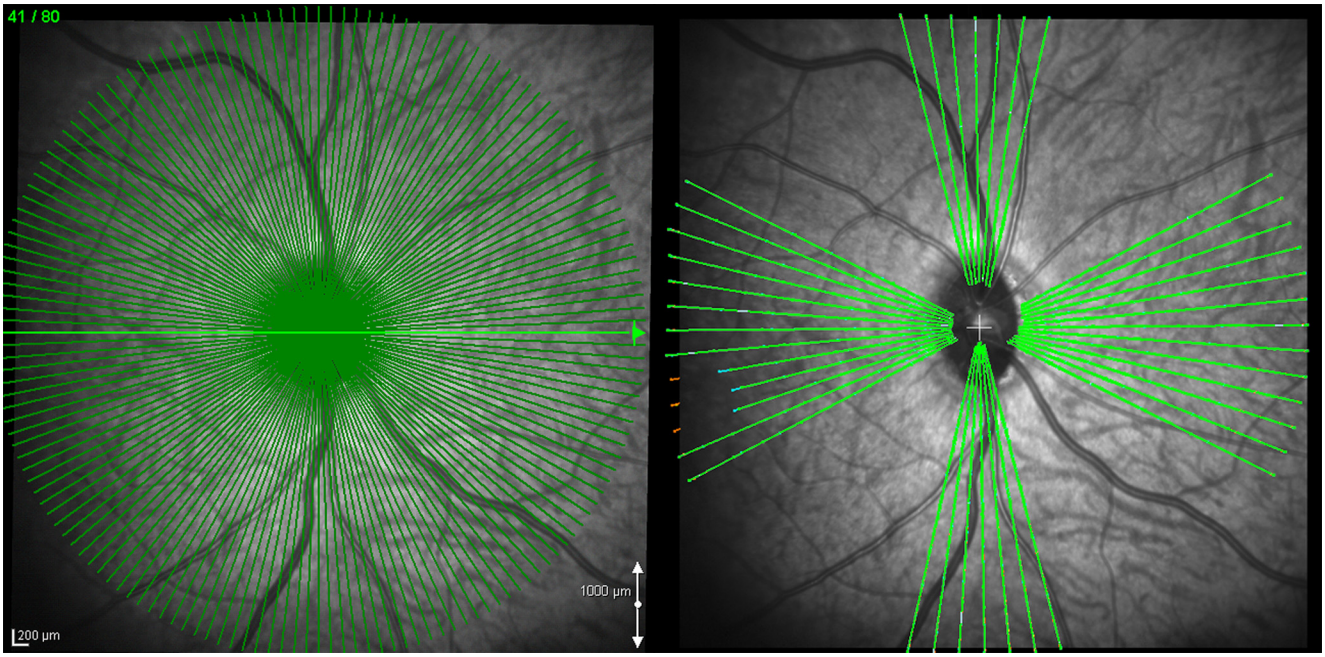

Figure 2. SD-OCT data set acquisition and delineation. Of the 80 radial B-scans acquired in each 30° conventional or EDI SD-OCT ONH data set (*left*) a subset of 7 vertical and 13 horizontal B-scans were delineated for this study (*right*).

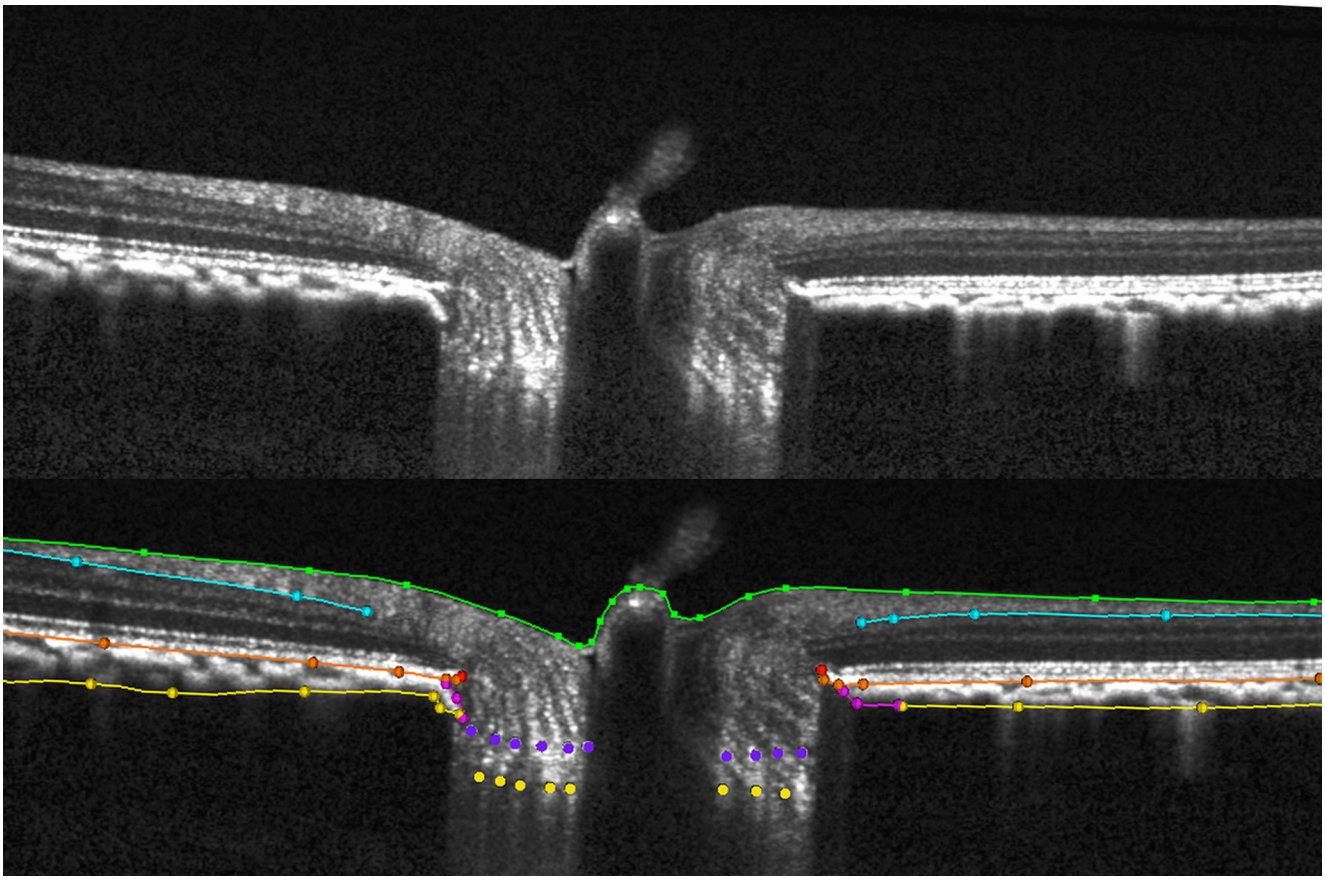

FIGURE 3. Landmark delineation in a normal eye. Raw representative EDI SDSOCT ONH B-scan (*top*). Same SD-OCT ONH B-scan showing delineations (*bottom*): *green*: internal limiting membrane; *blue*: posterior surface of RNFL; *orange*: posterior surface of retinal pigment epithelium/Bruch's membrane complex; *red*: neural canal opening (NCO), the innermost termination of the RPE/BM complex; *pink*: border tissue of Elschnig, located at the innermost termination of choroidal signal; *purple*: ALCS; *gold*: PLCS; and *yellow*: anterior scleral surface.

eyes of three randomly selected NHPs, to compare the intradelineator reproducibility of laminar visualization and ONH parameters in the conventional and EDI SD-OCT data sets.

Statistical Analyses

The effects of image type (conventional versus EDI), treatment (control versus EG), and quadrants (S, I, N, and T) on the number of delineated ALCS and PLCS subregions were analyzed by ANOVA. Poisson regression was used to fit the delineated ALCS and PLCS data, and significance was tested with the χ^2 test. Two-tailed, paired *t*-tests were used to compare the ONH parameters generated from conventional and EDI data sets. For all tests, $P < 0.005$ was considered to be significant to account for the number of comparisons in each analysis and maintain an overall type 1 error rate of approximately 0.05. To test intradelineator variability, the effects of image type (conventional versus EDI) and delineation day were assessed overall and for each parameter in a separate ANOVA ($P < 0.005$). Statistical analyses were performed with one of two software packages (R statistical software; R Foundation for Statistical Computing, Vienna, Austria, or Excel; Microsoft Corporation, Redmond, WA).

Results

Conventional and EDI ONH data sets were obtained in both eyes of 14 animals with unilateral EG on a single postlaser imaging day that occurred at a postlaser interval specific to each EG eye (Table 1). Imaging day SD-OCT-detected RNFL change (relative to baseline) within the conventional RNFL circle scans of the 12 EG eyes for which both baseline and imaging day values were available ranged from +9% (thickening) to −28% (thinning), with a median value of +1% (Table 1). Of these 12 EG eyes, 11 had less than 10% RNFL loss, and 1 had 28% RNFL loss relative to their own baseline values. Imaging day SD-OCT RNFLT in the two remaining EG eyes that lacked baseline values was 33% and 68% thinner than that in the contralateral normal eyes. Thus, although most of the EG eyes were imaged with EDI at an early stage in the neuropathy, three eyes (NHPs 12, 13, and 14) demonstrated moderate to severe levels of RNFL thinning.

Delineated ALCS and PLCS Points without Regard to Subregion. Delineated ALCS and PLCS points in the conventional and EDI data sets of all 28 eyes are depicted in Figures 6 and 7. Qualitative inspection of these data suggests that adoption of EDI results in only a minimal improvement in ALCS detection but that there can be a marked improvement in PLCS detection.

Delineated Lamina Cribrosa Subregions by Image Type. When eyes were considered without regard to treatment status, the number of delineated laminar subregions was larger in the EDI scans than in the conventional scans for both the ALCS (EDI, 37 ± 7 vs. conventional, 29 ± 11; 28% difference; $P < 0.0001$) and PLCS (EDI, 26 ± 11 vs. conventional, 8 ± 10; 225% difference; $P < 0.0001$). These data suggest that EDI imaging significantly enhanced laminar visualization in both control and EG eyes.

Delineated Lamina Cribrosa Subregions in Control and EG Eyes. The effects of treatment, image type, and their interactions are listed in Table 2. For both the ALCS and PLCS, the number of delineated subregions was significantly larger in

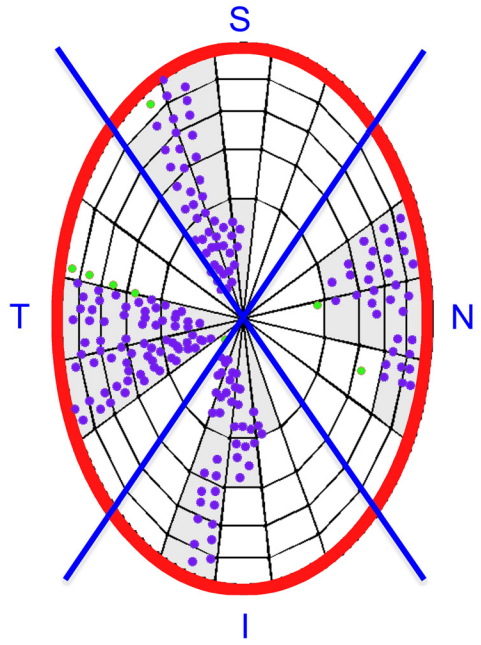

FIGURE 4. Determination of delineated ALCS subregions. ACLS points (*purple glyphs*) are projected onto the plane of an ellipse (*red outline*) best fit to the NCO. The NCO ellipse is subdivided into 100 subregions of equal area.[20] Subregions where two or more delineated points are present are maintained for analysis as delineated regions (*light gray*). Points within regions where less than two points were delineated (*green glyphs*) were not included in further analyses. Each subregion is assigned to the superior, inferior, nasal, or temporal quadrants (*blue lines*). The same method was applied to the posterior lamina cribrosa subregions.

the EDI data sets for both the control (ALCS, 22%; $P = 0.0016$; PLCS, 133%; $P < 0.0001$) and glaucomatous (ALCS, 33%; $P < 0.0001$; PLCS, 360%; $P < 0.0001$) eyes. Although the relative improvement achieved by EDI in control versus EG eyes did not achieve statistical significance for ALCS delineation ($P = 0.30$, ANOVA), EDI improvement in PLCS delineation was significantly greater in the EG than in the control eyes ($P < 0.0001$). These data indicate that EDI enhancement of PLCS visualization is greater in EG than in control eyes.

In the conventional SD-OCT ONH data sets, the number of delineated subregions was significantly less in the EG (5 ± 6) than in the control eyes (12 ± 12) for the PLCS ($P < 0.0001$) but not the ALCS ($P = 0.054$). However, although there were fewer delineated subregions in the EDI data sets of the EG than in those of the control eyes, these differences did not achieve significance. These data suggest that PLCS delineation by conventional SD-OCT was diminished in the EG compared with the control eyes.

Delineated Lamina Cribrosa Subregions by Quadrant. Because we delineated twice as many scans oriented close to the horizontal plane as close to the vertical sections, the number of nasal and temporal ALCS and PLCS delineated subregions was greatest for both imaging types (Table 3). However, the number of delineated ALCS subregions significantly increased in the EDI compared with the conventional data sets for the superior (conventional, 4 ± 3 vs. EDI, 7 ± 3) and inferior (conventional, 4 ± 3 vs. EDI, 6 ± 3) quadrants, whereas the number of delineated PLCS subregions significantly increased in the EDI compared with the conventional data sets for all four quadrants (superior, conventional 1 ± 2 vs. EDI 4 ± 3; inferior, conventional 1 ± 1 vs. EDI 3 ± 3; nasal, conventional 3 ± 5 vs. EDI 9 ± 4; and temporal, conventional 4 ± 4 vs. EDI 10 ± 3). These data suggest that EDI enhancement of ALCS visualization may be limited to the superior and inferior quadrants, whereas PLCS enhancement occurs in all four quadrants.

When the above data were separately assessed in control and EG eyes (Table 4), the improvement in ALCS delineation using EDI was significant for both control and EG eyes in the superior quadrant only. However, the number of delineated PLCS subregions significantly increased in the EDI compared with the conventional data sets in all four quadrants of both the control and EG eyes. This improvement in PLCS visualization was significantly greater in the EG than in the control eyes for the nasal ($P = 0.001$) and temporal ($P = 0.004$) quadrants only. Taken together, these data suggest that EDI enhancement of laminar visualization is greatest for PLCS within the nasal and temporal quadrants of EG eyes.

Conventional versus EDI Values for All Other ONH and RNFL Parameters. To test the hypothesis that EDI imaging would not affect landmark delineation for other representative ONH and RNFL parameters, we compared the mean value of each parameter in the conventional ($n = 28$) versus EDI ($n = 28$) data sets (Table 5). Only the parameters ALCS depth (mean difference, 8%; range, 1%–21%) and PLCS depth (mean difference, 9%; range, 1%–20%) demonstrated significant differences between the conventional and EDI data sets ($P < 0.005$, *t*-test). For both parameters, the mean value was larger (i.e., deeper, or more posterior) in the EDI data sets.

However, when we reanalyzed these two parameters using only those laminar regions for each eye that were delineated in both the conventional and EDI data sets (shared laminar regions), there was no significant difference between the EDI and conventional data for ALCS depth (conventional, 221 μm vs. EDI, 230 μm; $P = 0.041$); Contrary to the ALCS, the shared PLCS depth value remained significantly greater in the EDI than in the conventional data sets, (conventional, 320 μm vs. EDI, 346 μm; $P = 0.0002$). In this regard, of the 15 individual eyes, which had shared PLCS areas, in 14 of 15, the EDI PLCS depth was greater than the standard value, and 7 had a difference greater than 10% between the shared EDI and the shared standard PLCS depth.

Intradelineator Reproducibility for All Parameters in the Conventional and EDI Data Sets from Both Eyes of three Animals. Neither delineation day nor the interaction between delineation day and image type was significant by ANOVA. These data suggest that interday differences in delineation were not a significant source of variability, nor were they better or worse in conventional versus EDI data sets (Table 6).

The mean maximum interday difference for delineated ALCS subregions in conventional data sets was 5 (range, 2–9) and in EDI data sets was 6 (range, 3–12). The mean difference for delineated ALCS subregions in conventional data sets was 17% (range, 7%–31%) and in EDI data sets was 16% (range, 8%–32%). The average maximum intersession difference for delineated PLCS subregions in conventional data sets was 4 (range, 0–7) and in EDI data sets was 6 (range, 3–7). The mean difference for delineated PLCS subregions in conventional data sets was 50% (range, 0%–88%) and in the EDI data sets was 23% (range, 12%–27%). Taken together, these data suggest that the reproducibility of the PLCS in EDI data sets was enhanced compared with that in conventional data sets, although the small number of delineated PLCS points in the conventional images may limit the importance of this finding. The mean difference for all parameters in both the conventional and EDI data sets was less than 13%.

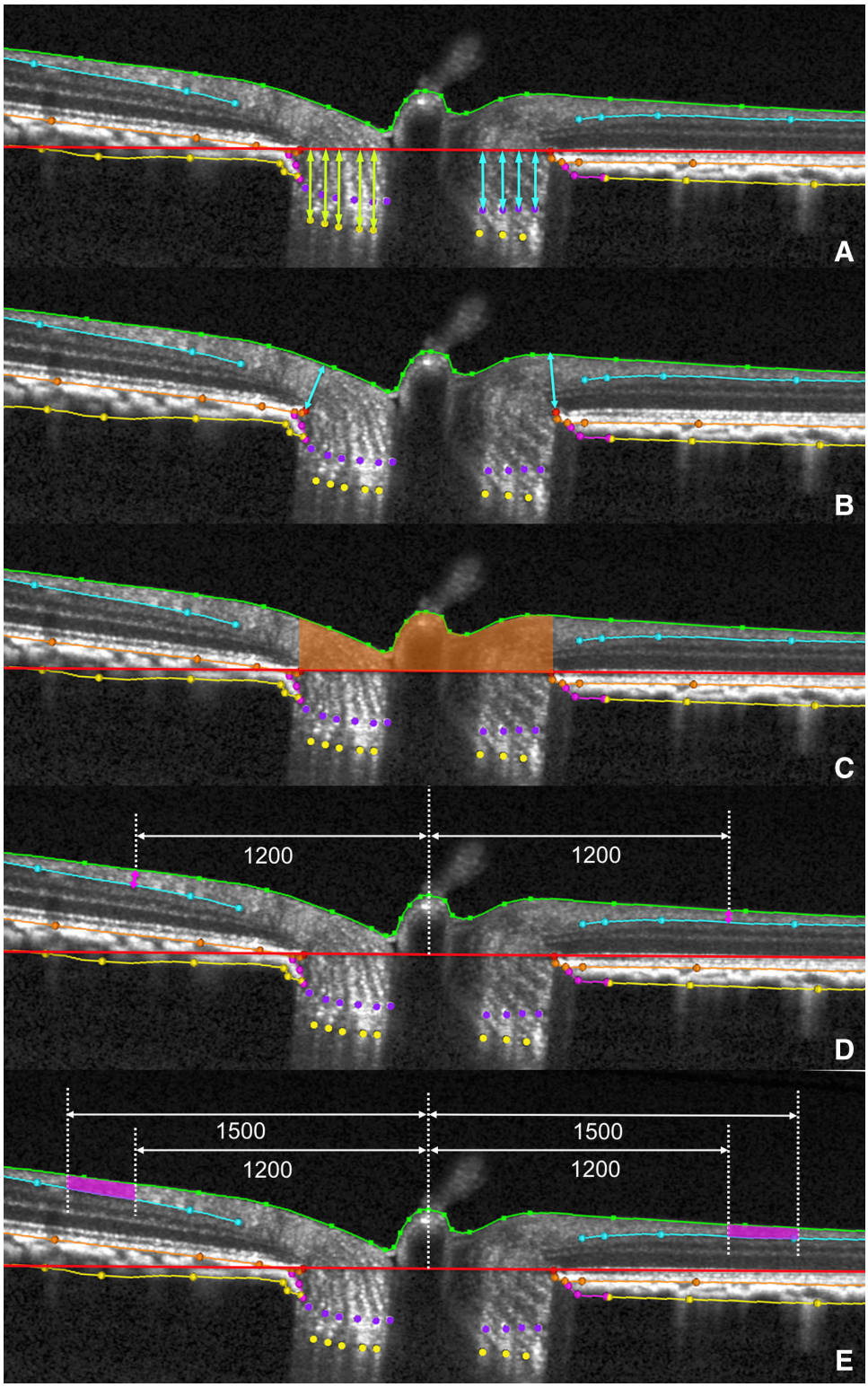

FIGURE 5. ONH and RNFL parameter definitions as measured within each B-scan. (**A**) PLCS depth (*light yellow-green arrows*) was measured at each delineated PLCS point as the perpendicular distance from the neural canal opening (NCO) reference plane (*red line* in the cross-section). ALCS depth (*light blue arrows*) was measured at each delineated ALCS point as the perpendicular distance from the NCO reference plane. (**B**) Rim width (*light blue arrows*) was measured at each delineated NCO point (*red*) as the minimum distance to the ILM (*green B-spline line*). (**C**) Rim area was measured within each B-scan as the area contained within the NCO reference plane section line (*red*), the ILM (*green B-spline line*) and perpendicular projections from each NCO point (*red*). These projections are the left and right borders of the rust-colored area. (**D**) RNFLT 1200 was measured on either side of the canal at ILM points that were 1200 μm from the centroid of the 80 delineated NCO points (the NCO centroid). *Central white vertical dotted line*: projection of the NCO centroid. RNFLT at each ILM point was the minimum distance (*pink arrow*) between the ILM and the posterior (outer) RNFL boundary (*light blue B-spline line*). (**E**) RNFL area (*pink*) was generated on either side of the canal from the area contained within the 1200- and 1500-μm ILM point perpendiculars (*peripheral vertical dotted white lines*), the ILM (*green B-spline line*), and the posterior (outer) RNFL boundary (*light blue B-spline line*).

DISCUSSION

In this study, we quantified the regional extent of SD-OCT laminar cribrosa surface delineation in a subset of vertical and horizontal radial B-scans from both ONHs of 14 NHPs with unilateral EG. Specifically, we tested the hypothesis that the EDI mode of SD-OCT imaging would improve the visibility of the anterior and posterior lamina cribrosa surfaces compared with conventional SD-OCT imaging. The principal findings are as follows. First, when evaluated without regard to treatment status, the number of delineated LC subregions was significantly larger for the EDI compared with the conventional data sets, for both the ALCS and PLCS. Second, when considering treatment status, we found that PLCS visualization in the conventional SD-OCT data sets was diminished in the EG compared to the control eyes, that EDI enhanced both control and

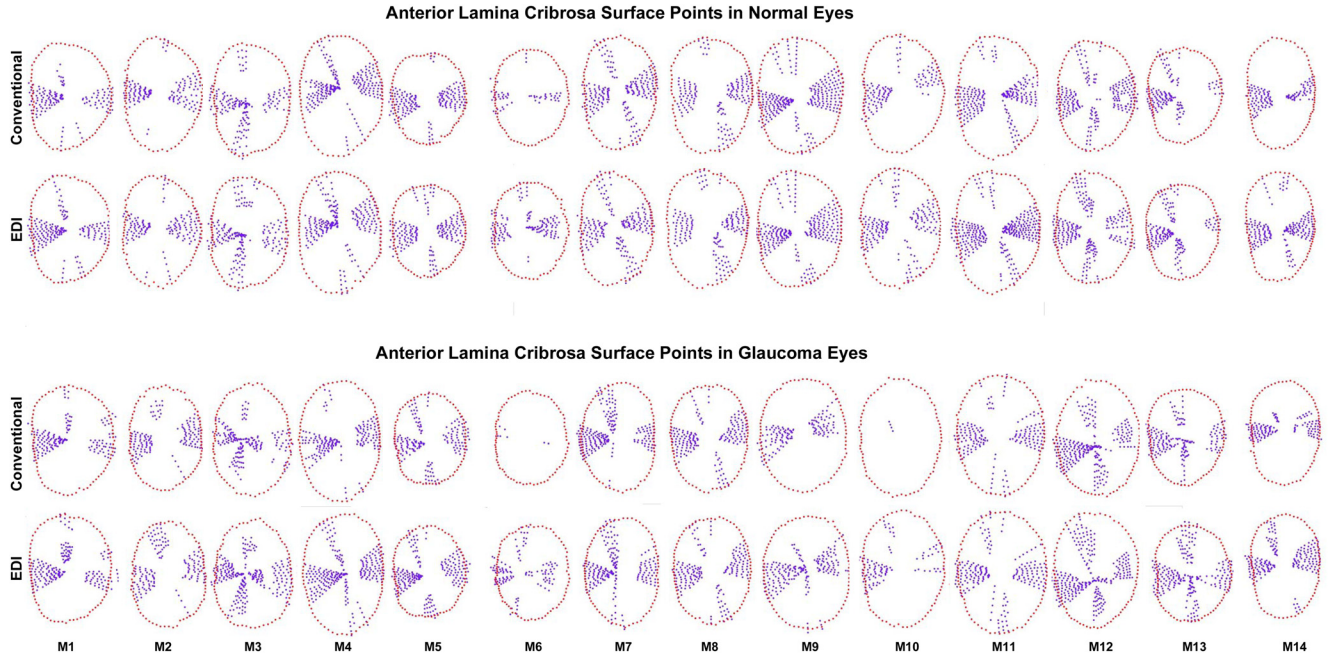

Figure 6. ALCS delineation within the central 7 vertical and 13 horizontal B-scans from conventional and EDI SD-OCT ONH data sets of the normal and EG eyes of each animal. ALCS points (*purple glyphs*) are projected onto the plane of the NCO (*red glyphs*) and displayed in right-eye configuration.

EG eye laminar visualization (for both the ALCS and PLCS), and that this enhancement was greater in the EG eyes. These results suggest that EDI does enhance the visibility of the lamina cribrosa, particularly of the posterior surface and especially in glaucomatous eyes. Third, apart from the extent of ALCS and PLCS delineation there were no significant differences in the value of other ONH parameters in EDI versus conventional data sets, except for PLCS depth, which was significantly deeper in the EDI data sets. This result suggests that, in addition to the improvement offered by EDI for LC visualization, there is no detriment to quantifying more anterior structures/layers.

Lee et al.[36] recently reported enhanced signal depth in EDI versus conventional vertical ONH B-scans of 35 eyes of 35 patients (10 normal, 7 glaucoma suspect, and 18 glaucoma eyes). Using EDI SD-OCT, they qualitatively judged that the posterior lamina cribrosa was visible in all 35 EDI B-scans, but it was difficult to discriminate the difference between decreas-

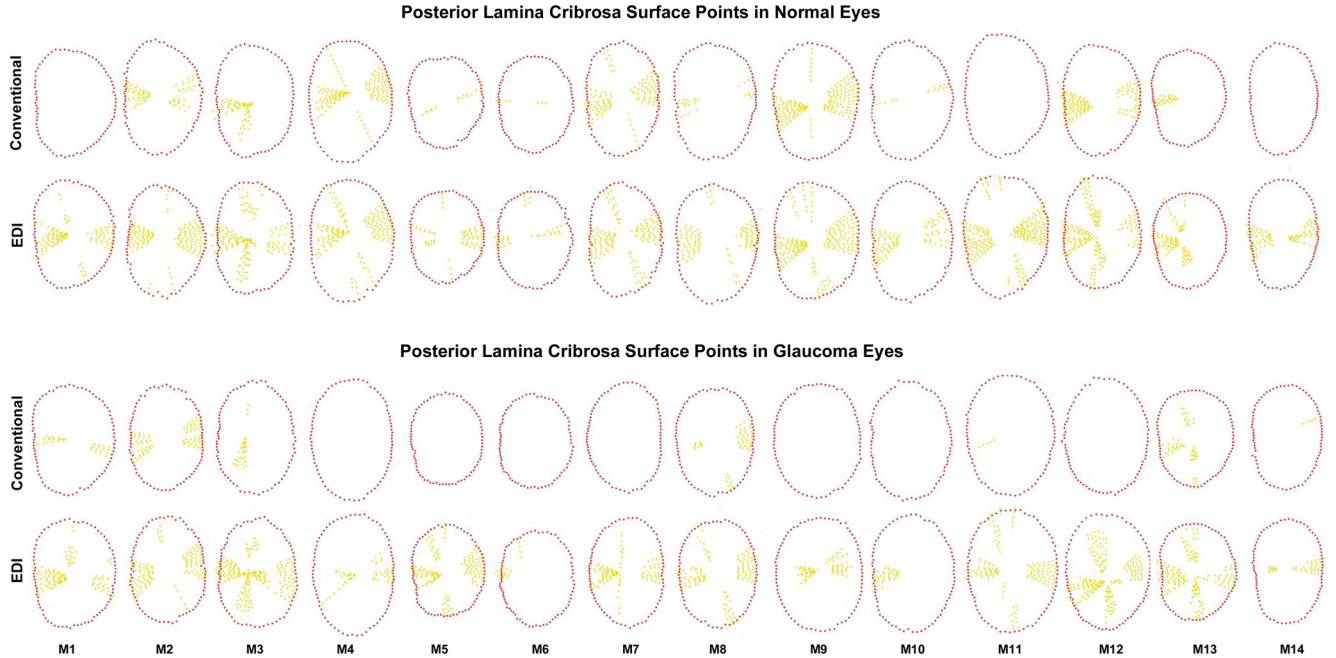

Figure 7. PLCS delineation within the central 7 vertical and 13 horizontal B-scans from conventional and EDI SD-OCT ONH data sets of the normal and EG eyes of each animal. PLCS points (*yellow* glyphs) are projected onto the plane of the NCO (*red* glyphs) and displayed in right-eye configuration.

Table 2. Delineated Lamina Cribrosa Subregions in Normal and EG Eyes

	Control Eyes			Glaucomatous Eyes		
	Image Type*			Image Type		
	Conventional (Mean ± SD)	EDI (Mean ± SD)	*P*	Conventional (Mean ± SD)	EDI (Mean ± SD)	*P*
ALCS	31 ± 9	38 ± 6	**0.0016**	27 ± 12	36 ± 8	**<0.0001**
PLCS†	12 ± 12	28 ± 10	**<0.0001**	5 ± 6	23 ± 12	**<0.0001**

Bold: significant difference between conventional and EDI imaging modes.
* For both image types, the number of delineated subregions with at least two points was reported.
† For the PLCS, the interaction between treatment and image type is significant ($P < 0.005$, ANOVA).

ing contrast due to the changes within tissue (i.e., at the posterior end of the lamina cribrosa) versus declining signal strength in either SD-OCT imaging mode. Although we did not compare the depth of EDI versus standard signal penetration in our study, it expands the assessment of anterior and posterior laminar visualization to all four quadrants (7 vertical and 13 horizontal B-scans) and utilizes a previously reported strategy for laminar visualization quantification[20] that can become the framework for similar studies regardless of the instruments, imaging wavelengths, or visualization strategies being compared. Using this strategy, our findings support those of Lee et al.[36] in that PLCS visualization was greater in the EDI than in the conventional B-scans from all four quadrants of the studied eyes.

Although there are no quantitative data that compare SD-OCT visualization of the lamina in normal and glaucomatous human eyes, it has been our impression that SD-OCT lamina cribrosa visualization is enhanced in glaucomatous human eyes. However, in the NHP eyes in this report, there were no differences between EG and control eyes in the regional extent of ALCS visualization, with the conventional or the EDI scan modes. PLCS visualization was in fact significantly less in the EG eyes than in their fellow control eyes in both EDI and conventional data sets. Thus, it is a potentially important benefit that the enhancement provided by EDI over conventional SD-OCT mode was significant for the PLCS and greatest in glaucomatous eyes. However, it should be noted that the majority of glaucomatous eyes in this study were at an early stage of neuropathy.

It is possible that the lack of improvement in ALCS visualization in the glaucomatous eyes may be due to the relatively early stage of glaucomatous damage at the time of imaging in most eyes. On the day of EDI imaging, the peripapillary SD-OCT circle scan measurements of RNFLT were actually greater in the EG eyes of 7 of the 14 animals (NHPs 1–4, 6, 8, and 10), minimally decreased in 3 animals (NHPs 5, 7, and 11), and mildly decreased in 4 animals (NHPs 9, 12, 13, and 14). However, the difference in ALCS and PLCS visualization between the normal and EG eyes of our more damaged animals (NHPs 12, 13, and 14; Figs. 6, 7) are also not profound.

Table 3. Delineated Lamina Cribrosa Subregions by Quadrant

		Image Type		
Landmark	Quadrant	Conventional (Mean ± SD)	EDI (Mean ± SD)	*P*
ALCS	Superior	4 ± 3	7 ± 3	**<0.0001**
	Inferior	4 ± 3	6 ± 3	**0.0004**
	Nasal	10 ± 4	12 ± 3	0.07
	Temporal	11 ± 4	13 ± 2	0.09
PLCS	Superior	1 ± 2	4 ± 3	**<0.0001**
	Inferior	1 ± 1	3 ± 3	**<0.0001**
	Nasal	3 ± 5	9 ± 4	**<0.0001**
	Temporal	4 ± 4	10 ± 3	**<0.0001**

Bold: significant difference between conventional and EDI.

Taken together, our data suggest that laminar visualization is compromised rather than enhanced in glaucomatous NHP eyes at all stages of damage, although this observation must be confirmed in a larger number of eyes, over more advanced stages of damage and may not apply to human glaucoma. In work by Strouthidis et al.,[20] no significant difference in the number of the marked lamina cribrosa sectors was found between two baseline time points and two glaucoma time points in nine glaucomatous monkeys. It is possible that, even in the face of eventual prelaminar tissue thinning, which should improve laminar visualization, the profound outward remodeling of the laminar cribrosa insertions[15] and the laminar transition zone region that our collaborators[40] and others[41] have reported lead to reflectivity changes within the tissues of the anterior and posterior laminar borders, making them more difficult to discern. This hypothesis warrants further study.

We also assessed the potential differences between conventional and EDI scanning modes for a wide array of previously described[20] ONH and RNFL parameters. We found significant differences between EDI and conventional values for only ALCS and PLCS depths (measured relative to the NCO reference plane). After additional analysis in which only the laminar subregions that were present in both the conventional and EDI data sets of each eye were included, only PLCS depth was found to be different (more posterior) by EDI. The lack of change in all the other parameters is important because it suggests that any compromise of inner retinal and prelaminar ONH imaging that may be present in EDI data sets (see the introduction) does not significantly affect their quantification.

The fact that shared PLCS depth was significantly deeper in 14 of the 15 eyes in which it could be assessed suggests that the enhanced visualization depth in EDI versus conventional datasets may not only provide regional expansion of PLCS delineation capability, but a more accurate determination of the axial position of the PLCS. We believe that EDI PLCS visualization represents a more accurate visualization than does the conventional SD-OCT mode, as would be predicted on the basis of the physics underlying the EDI method. That is, in SD-OCT signal strength declines with distance from the 0 delay point (relative to the time of flight of the reference beam)—a concept known as depth degeneracy. Signal strength also declines due to scatter and absorption of the source through the tissue sample. This latter limitation is operative for both conventional and EDI modes but in the EDI mode, the direction of depth degeneracy is inversely related to the conventional mode, thus predicting improvement in signal strength (and possibly discrimination) of the deeper structures. That our

TABLE 4. Delineated Lamina Cribrosa Subregions by Quadrant and Treatment

		Control Eyes			Glaucoma Eyes		
		Image Type			Image Type		
Landmark	Quadrant	Conventional (Mean ± SD)	EDI (Mean ± SD)	*P*	Conventional (Mean ± SD)	EDI (Mean ± SD)	*P*
ALCS	Superior	4 ± 3	7 ± 2	**0.004**	4 ± 3	7 ± 3	**<0.0001**
	Inferior	4 ± 3	6 ± 3	0.027	3 ± 3	5 ± 3	0.008
	Nasal	11 ± 4	13 ± 3	0.27	10 ± 4	11 ± 3	0.15
	Temporal	12 ± 3	13 ± 3	0.45	11 ± 5	13 ± 2	0.10
PLCS	Superior	1 ± 2	4 ± 3	**<0.0001**	<1	4 ± 3	**<0.0001**
	Inferior	1 ± 1	4 ± 3	**<0.0001**	1 ± 1	3 ± 3	**<0.0001**
	Nasal*	5 ± 6	10 ± 4	**<0.0001**	2 ± 3	8 ± 4	**<0.0001**
	Temporal*	6 ± 5	11 ± 3	**<0.0001**	2 ± 3	9 ± 4	**<0.0001**

Bold: significant difference between conventional and EDI ($P < 0.005$, ANOVA).

* Interaction between treatment and Image type is significant for this landmark and quadrant ($P < 0.005$, ANOVA).

results find some degree of enhancement by EDI for lamina cribrosa delineation suggests that depth degeneracy does have some impact, although signal loss by other factors still poses limitations. It is hoped that longer wavelength sources (e.g., 1050 nm) may help in this regard.[42–45]

Our study is limited for the following reasons. First, as noted above, the PLCS delineations we report are not supported by histologic verification and should therefore be considered preliminary. Our previous study[29] provides histologic verification of conventional SD-OCT ALCS delineation. Within the single normal NHP ONH of that report, the PLCS was not felt to be visible in conventional SD-OCT B-scans. There has been no histologic confirmation that what has been delineated as the PLCS in this and previous reports[29] is accurate.

Second, our study would have more strongly tested hypotheses regarding regional differences in laminar visibility had we delineated the complete subset of 40 radial B-scans that we usually delineate. We chose to limit this study to 7 vertical and 13 horizontal radial B-scans for the following reasons: First, it is commonly acknowledged that SD-OCT visualization of deep ONH anatomy is markedly diminished within the superior and inferior ONH quadrants by the overlying central retinal artery and its principle branches.[20] Our initial evaluation suggested that visualization within the superior and inferior quadrants would be only marginally improved by EDI imaging and, if present, such an improvement would probably be detectable within the central seven vertical B-scans where laminar delineation is least common. It is therefore interesting to note that the increase in delineated ALCS subregions by EDI was significantly greater in the superior–inferior than in the nasal–temporal quadrants. We also felt that because delineation of the lamina was more common within the nasal–temporal quadrants in conventional SD-OCT imaging, a larger delineated region might be necessary to detect smaller improvements in visualization in these quadrants. In this regard it is interesting to note that although there were small improvements in EDI visualization of the ALCS in the nasal temporal regions, these did not achieve significance, whereas for the PLCS the increase in delineated PLCS subregions was statistically significant in all four quadrants.

Our assessment of the larger group of ONH parameters (beyond the ALCS and PLCS) is limited to the overall data only and may thus have missed important regional differences in EDI versus conventional SD-OCT visualization. However, any systematic bias should have manifested in the overall measures. We also did not formally assess anterior versus posterior delineation differences in severely damage eyes in which profound posterior laminar deformation (very deep cupping) may re-

TABLE 5. Conventional versus EDI Values for All Other ONH and RNFL Parameters

Parameters	Conventional Imaging*	EDI Imaging*	Difference† (%)	*P*
ALCS depth, μm	231 (144–428)	244 (150–422)	8 (1–21)	**0.00315**
PLCS depth, μm‡	336 (252–495)	367 (282–528)	9 (1–20)	**<0.0001**
Shared ALCS depth, μm	221 (137–453)	230 (146–403)	7 (1–19)	0.0406
Shared PLCS depth, μm§	320 (244–482)	346 (275–515)	9 (2–16)	**0.0002**
NCO major, μm	1554 (1294–1731)	1554 (1304–1737)	1 (0–3)	0.86
NCO minor, μm	1105 (965–1238)	1107 (969–1264)	1 (0–4)	0.51
NCO area, μm^2	1.35 (1.0452–1.6638)	1.36 (1.0470–1.7235)	1 (0–4)	0.49
Rim width, μm	249 (72–360)	246 (68–354)	1 (0–6)	0.43
Rim area, μm^2	0.1978 (0.0137–0.3948)	0.1963 (0.012–0.3874)	2 (0–14)	0.0313
RNFLT 1200, μm	95 (45–126)	95 (52–121)	4 (0–15)	0.72
RNFL area, μm^2	0.0257 (0.0126–0.0343)	0.0253 (0.0113–0.0332)	5 (1–11)	0.07

See the Methods section and Figure 6 for a definition of these parameters.[20] Data are expressed as the mean (range). Bold: significant difference between the mean values in the conventional and EDI data sets ($P < 0.005$, paired *t*-test corrected for multiple comparisons).

* Mean and range for pooled data for each parameter in the $n = 28$ conventional and $n = 28$ EDI data sets.

† The difference for each parameter for each data set (data not shown) was defined as the absolute difference between the conventional and EDI values divided by the mean of the two values. The mean and range of the difference for the 28 individual conventional and EDI data sets are shown.

‡ Data for the 18 of 28 data sets that contained PLCS delineations within both image types are reported.

§ Data for 15 data sets that contained the shared PLCS subregions within both image types are reported.

Table 6. Intradelineator Reproducibility (n = 3 Delineation Days) for All Parameters within the Conventional and EDI Data Sets of Both Eyes of Three Animals

	Conventional Imaging		EDI Imaging	
Parameter	**Maximum Difference***	**Difference† (%)**	**Maximum Difference***	**Difference† (%)**
ALCS subregions	5 (2–9)	17 (7–31)	6 (3–12)	16 (8–32)
PLCS subregions	4 (0–7)	50 (0–88)	6 (3–7)	23 (12–27)
ALCS depth, μm	18 (5–32)	8 (2–14)	14 (3–24)	6 (1–10)
PLCS depth, μm	NA‡	NA‡	19 (11–27)	5 (3–7)
NCO major, μm	198 (136–298)	13 (9–21)	110 (41–227)	7 (2–15)
NCO minor, μm	68 (20–188)	6 (2–17)	81 (21–216)	7 (2–20)
NCO area, μm^2	0.0077 (0.0013–0.0120)	0.6 (0.1–0.9)	0.0051 (0.0016–0.0107)	0.4 (0.1–0.8)
Rim width, μm	4 (1–8)	2 (0–3)	3 (2–5)	1 (0–2)
Rim area, μm^2	0.0041 (0.0009–0.0098)	1.9 (0.2–3.5)	0.0032 (0.0010–0.0045)	1.6 (0.5–2.3)
RNFLT 1200, μm	8 (0–20)	8 (0–21)	7 (1–19)	7 (1–20)
RNFL area, μm^2	0.0021 (0.0001–0.0055)	8 (0.4–21)	0.0020 (0.0003–0.0056)	8 (1–22)

Mean and range for all six delineated eyes (both eyes of three animals) are shown.

* Maximum difference for each individual data set (data not shown) is the maximum between-day, pair-wise difference.

† Difference for an individual data set (data not shown) is the maximum difference divided by the mean value of three delineation days.

‡ Of the 18 data sets in this group, 10 did not have PLCS points.

quire even deeper positioning of the tissue sample. In such circumstances, prelaminar ONH and retinal imaging can be compromised by the limitations of the total scan depth, but may be especially problematic in the EDI mode with potential loss of sensitivity toward the more anterior tissue sample layers. Evaluation of regional and anterior to posterior differences in conventional and EDI SD-OCT ONH data sets in humans with glaucoma is therefore necessary.

Our assessment of effects on reproducibility of switching to EDI SD-OCT mode is limited to intradelineator reproducibility and does not include intersession acquisition variability. To have studied interimage session variability would have required delineation of EDI and conventional SD-OCT data sets acquired on two or three different imaging days and was beyond the scope of this study. Interimage session variability may be the most important determinant of the sensitivity and specificity of longitudinal change detection and will be the subject of a future report.

Finally, our study may have underestimated EDI visualization enhancement because EDI imaging has had the uncontrolled effect of enhancing conventional SD-OCT delineation by our delineator. It is our experience that the subtle EDI enhancements of ALCS and PLCS visualization serve to inform even masked delineators such that they begin to recognize anatomy in conventional SD-OCT data sets that they would not previously delineate. We expect that this effect may be operative in other studies based on manual delineation and that additional advances such as 1050 nm SD-OCT[42–45] and OCT signal compensation[24] may have similar unintended effects.

Acknowledgments

The authors thank Jonathan Grimm and Juan Reynaud for assistance with the software and hardware, Galen Williams and Erica Dyrud for assistance with the imaging, and Joanne Couchman for assistance with manuscript preparation and submission.

References

1. Quigley HA, Addicks EM. Chronic experimental glaucoma in primates, II: effect of extended intraocular pressure elevation on optic nerve head and axonal transport. *Invest Ophthalmol Vis Sci.* 1980;19:137–152.
2. Quigley HA, Addicks EM, Green WR, Maumenee AE. Optic nerve damage in human glaucoma, II: the site of injury and susceptibility to damage. *Arch Ophthalmol.* 1981;99:635–649.
3. Quigley HA, Guy J, Anderson DR. Blockade of rapid axonal transport: effect of intraocular pressure elevation in primate optic nerve. *Arch Ophthalmol.* 1979;97:525–531.
4. Quigley HA, Hohman RM, Addicks EM, Massof RW, Green WR. Morphologic changes in the lamina cribrosa correlated with neural loss in open-angle glaucoma. *Am J Ophthalmol.* 1983;95:673–691.
5. Girard MJ, Suh JK, Bottlang M, Burgoyne CF, Downs JC. Biomechanical changes in the sclera of monkey eyes exposed to chronic IOP elevations. *Invest Ophthalmol Vis Sci.* 2011;52:5656–5669.
6. Howell GR, Libby RT, Jakobs TC, et al. Axons of retinal ganglion cells are insulted in the optic nerve early in DBA/2J glaucoma. *J Cell Biol.* 2007;179:1523–1537.
7. Bianchi-Marzoli S, Rizzo JF 3rd, Brancato R, Lessell S. Quantitative analysis of optic disc cupping in compressive optic neuropathy. *Ophthalmology.* 1995;102:436–440.
8. Jonas JB, Berenshtein E, Holbach L. Anatomic relationship between lamina cribrosa, intraocular space, and cerebrospinal fluid space. *Invest Ophthalmol Vis Sci.* 2003;44:5189–5195.
9. Ren R, Wang N, Li B, Li L, Gao F, Xu X, Jonas JB. Lamina cribrosa and peripapillary sclera histomorphometry in normal and advanced glaucomatous Chinese eyes with various axial length. *Invest Ophthalmol Vis Sci.* 2009;50:2175–2184.
10. Hernandez MR, Andrzejewska WM, Neufeld AH. Changes in the extracellular matrix of the human optic nerve head in primary open-angle glaucoma. *Am J Ophthalmol.* 1990;109:180–188.
11. Agapova OA, Yang P, Wang WH, et al. Altered expression of 3 alpha-hydroxysteroid dehydrogenases in human glaucomatous optic nerve head astrocytes. *Neurobiol Dis.* 2003;14:63–73.
12. Yang H, Downs JC, Bellezza AJ, Thompson H, Burgoyne CF. 3-D Histomorphometry of the normal and early glaucomatous monkey optic nerve head: prelaminar neural tissues and cupping. *Invest Ophthalmol Vis Sci.* 2007;48:5068–5084.
13. Yang H, Downs JC, Girkin C, et al. 3-D histomorphometry of the normal and early glaucomatous monkey optic nerve head: lamina cribrosa and peripapillary scleral position and thickness. *Invest Ophthalmol Vis Sci.* 2007;48:4597–4607.
14. Bellezza AJ, Rintalan CJ, Thompson HW, Downs JC, Hart RT, Burgoyne CF. Deformation of the lamina cribrosa and anterior scleral canal wall in early experimental glaucoma. *Invest Ophthalmol Vis Sci.* 2003;44:623–637.
15. Yang H, Williams G, Downs JC, et al. Posterior (outward) migration of the lamina cribrosa and early cupping in monkey experimental glaucoma. *Invest Ophthalmol Vis Sci.* 2011;52:7109–7121.
16. Tan O, Chopra V, Lu AT, et al. Detection of macular ganglion cell loss in glaucoma by Fourier-domain optical coherence tomography. *Ophthalmology.* 2009;116:2305–2314 e2301–2302.
17. Kotera Y, Hangai M, Hirose F, Mori S, Yoshimura N. Three-dimensional imaging of macular inner structures in glaucoma by using

spectral-domain optical coherence tomography. *Invest Ophthalmol Vis Sci.* 2011;52:1412–1421.

18. Kim JS, Ishikawa H, Gabriele ML, et al. Retinal nerve fiber layer thickness measurement comparability between time domain optical coherence tomography (OCT) and spectral domain OCT. *Invest Ophthalmol Vis Sci.* 2010;51:896–902.
19. Schulze A, Lamparter J, Pfeiffer N, Berisha F, Schmidtmann I, Hoffmann EM. Diagnostic ability of retinal ganglion cell complex, retinal nerve fiber layer, and optic nerve head measurements by Fourier-domain optical coherence tomography. *Graefes Arch Clin Exp Ophthalmol.* 2011;249:1039–1045.
20. Strouthidis NG, Fortune B, Yang H, Sigal IA, Burgoyne CF. Longitudinal change detected by spectral domain optical coherence tomography in the optic nerve head and peripapillary retina in experimental glaucoma. *Invest Ophthalmol Vis Sci.* 2011;52:1206–1219.
21. Sung KR, Na JH, Lee Y. Glaucoma diagnostic capabilities of optic nerve head parameters as determined by Cirrus HD optical coherence tomography. *J Glaucoma.* Published online June 1, 2011.
22. Mansoori T, Viswanath K, Balakrishna N. Correlation between peripapillary retinal nerve fiber layer thickness and optic nerve head parameters using spectral domain optical coherence tomography. *J Glaucoma.* 2010;19:604–608.
23. Li S, Wang X, Wu G, Wang N. Evaluation of optic nerve head and retinal nerve fiber layer in early and advance glaucoma using frequency-domain optical coherence tomography. *Graefes Arch Clin Exp Ophthalmol.* 2010;248:429–434.
24. Girard MJ, Strouthidis NG, Ethier CR, Mari JM. Shadow removal and contrast enhancement in optical coherence tomography images of the human optic nerve head. *Invest Ophthalmol Vis Sci.* 2011;52:7738–7748.
25. Kagemann L, Ishikawa H, Wollstein G, et al. Ultrahigh-resolution spectral domain optical coherence tomography imaging of the lamina cribrosa. *Ophthalmic Surg Lasers Imaging.* 2008;39:S126–S131.
26. Inoue R, Hangai M, Kotera Y, et al. Three-dimensional high-speed optical coherence tomography imaging of lamina cribrosa in glaucoma. *Ophthalmology.* 2009;116:214–222.
27. Agoumi Y, Sharpe GP, Hutchison DM, Nicolela MT, Artes PH, Chauhan BC. Laminar and prelaminar tissue displacement during intraocular pressure elevation in glaucoma patients and healthy controls. *Ophthalmology.* 2011;118:52–59.
28. Strouthidis NG, Yang H, Reynaud J, et al. Comparison of clinical and spectral domain optical coherence tomography optic disc margin anatomy. *Invest Ophthalmol Vis Sci.* 2009;50:4709–4718.
29. Strouthidis NG, Grimm J, Williams G, Cull G, Wilson DJ, Burgoyne CF. A comparison of optic nerve head morphology viewed by spectral domain optical coherence tomography and by serial histology. *Invest Ophthalmol Vis Sci.* 2010;51:1464–1474.
30. Fortune B, Yang H, Strouthidis NG, et al. The effect of acute intraocular pressure elevation on peripapillary retinal thickness, retinal nerve fiber layer thickness and retardance. *Invest Ophthalmol Vis Sci.* 2009;50:4719–4726.
31. Strouthidis NG, Fortune B, Yang H, Sigal IA, Burgoyne CF. Effect of acute intraocular pressure elevation on the monkey optic nerve head as detected by spectral domain optical coherence tomography. *Invest Ophthalmol Vis Sci.* 2011;52:9431–9437.
32. Spaide RF, Koizumi H, Pozzoni MC. Enhanced depth imaging spectral-domain optical coherence tomography. *Am J Ophthalmol.* 2008;146:496–500.
33. Margolis R, Spaide RF. A pilot study of enhanced depth imaging optical coherence tomography of the choroid in normal eyes. *Am J Ophthalmol.* 2009;147:811–815.
34. Imamura Y, Iida T, Maruko I, Zweifel SA, Spaide RF. Enhanced depth imaging optical coherence tomography of the sclera in dome-shaped macula. *Am J Ophthalmol.* 2011;151:297–302.
35. Reibaldi M, Boscia F, Avitabile T, et al. Enhanced depth imaging optical coherence tomography of the choroid in idiopathic macular hole: a cross-sectional prospective study. *Am J Ophthalmol.* 2011;151:112–117, e112.
36. Lee EJ, Kim TW, Weinreb RN, Park KH, Kim SH, Kim DM. Visualization of the lamina cribrosa using enhanced depth imaging spectral-domain optical coherence tomography. *Am J Ophthalmol.* 2011;152:87–95.e1.
37. Pederson JE, Gaasterland DE. Laser-induced primate glaucoma, I: progression of cupping. *Arch Ophthalmol.* 1984;102:1689–1692.
38. Downs JC, Yang H, Girkin C, et al. 3-D Histomorphometry of the normal and early glaucomatous monkey optic nerve head: neural canal and subarachnoid space architecture. *Invest Ophthalmol Vis Sci.* 2007;48:3195–3208.
39. Strouthidis NG, Yang H, Fortune B, Downs JC, Burgoyne CF. Detection of optic nerve head neural canal opening within histomorphometric and spectral domain optical coherence tomography data sets. *Invest Ophthalmol Vis Sci.* 2009;50:214–223.
40. Roberts MD, Grau V, Grimm J, et al. Remodeling of the connective tissue microarchitecture of the lamina cribrosa in early experimental glaucoma. *Invest Ophthalmol Vis Sci.* 2009;50:681–690.
41. Nguyen JV, Soto I, Kim KY, et al. Myelination transition zone astrocytes are constitutively phagocytic and have synuclein dependent reactivity in glaucoma. *Proc Natl Acad Sci U S A.* 2011;108:1176–1181.
42. Puvanathasan P, Forbes P, Ren Z, Malchow D, Boyd S, Bizheva K. High-speed, high-resolution Fourier-domain optical coherence tomography system for retinal imaging in the 1060 nm wavelength region. *Opt Lett.* 2008;33:2479–2481.
43. Hofer B, Povazay B, Unterhuber A, et al. Fast dispersion encoded full range optical coherence tomography for retinal imaging at 800 nm and 1060 nm. *Opt Express.* 2010;18:4898–4919.
44. Eigenwillig CM, Klein T, Wieser W, Biedermann BR, Huber R. Wavelength swept amplified spontaneous emission source for high speed retinal optical coherence tomography at 1060 nm. *J Biophotonics.* 2011;4:552–558.
45. Huber R, Adler DC, Srinivasan VJ, Fujimoto JG. Fourier domain mode locking at 1050 nm for ultra-high-speed optical coherence tomography of the human retina at 236,000 axial scans per second. *Opt Lett.* 2007;32:2049–2051.